HHS Public Access

Author manuscript

Cell. Author manuscript; available in PMC 2020 May 16.

Published in final edited form as:

Cell. 2019 May 16; 177(5): 1252–1261.e13. doi:10.1016/j.cell.2019.03.050.

Structural mechanism of EMRE-dependent gating of the human mitochondrial calcium uniporter

Yan Wang[1,2], **Nam X. Nguyen**[1,2], **Ji She**[1,2], **Weizhong Zeng**[1,2], **Yi Yang**[1,2], **Xiao-chen Bai**[2,3,*], and **Youxing Jiang**[1,2,4,*]

[1]Howard Hughes Medical Institute and Department of Physiology, University of Texas Southwestern Medical Center, Dallas, Texas, USA

[2]Department of Biophysics, University of Texas Southwestern Medical Center, Dallas, Texas, USA

[3]Department of Cell Biology, University of Texas Southwestern Medical Center, Dallas, Texas, USA

[4]Lead Contact

Summary:

Mitochondrial calcium uptake is crucial to the regulation of eukaryotic Ca^{2+} homeostasis and is mediated by the mitochondria calcium uniporter (MCU). While MCU alone can transport Ca^{2+} in primitive eukaryotes, metazoans require an essential single membrane-spanning auxiliary component called EMRE to form functional channels; however, the molecular mechanism of EMRE regulation remains elusive. Here we present the cryo-EM structure of the human MCU/EMRE complex, which defines the interactions between MCU and EMRE as well as pinpoints the juxtamembrane loop of MCU and extended linker of EMRE as the crucial elements in the EMRE-dependent gating mechanism among metazoan mitochondrial calcium uniporters. The structure also features the dimerization of two MCU/EMRE complexes along an interface at the N-terminal domain (NTD) of human MCU that is a hotspot for post-translational modifications. Thus, the human MCU/EMRE complex, which constitutes the minimal channel components among metazoans, provides a framework for future mechanistic studies on MCU.

LS In brief

Structural analysis of the complex responsible for calcium import into human mitochondria shows how transporter gating is regulated.

[*]Correspondence to: Youxing Jiang, Ph.D., Department of Physiology, UT Southwestern Medical Center, 5323 Harry Hines Blvd., Dallas, Texas 75390-9040, Tel. 214 645-6027; Fax. 214 645-6042; youxing.jiang@utsouthwestern.edu; Xiao-chen Bai, Ph.D., Department of Biophysics, UT Southwestern Medical Center, 5323 Harry Hines Blvd., Dallas, Texas 75390-8816, Tel. 214 648-6089; xiaochen.bai@utsouthwestern.edu.

Author contributions: Y.W., N.X.N., and Y.J. conceived the study. Y.W., N.X.N., Y.J., and X.B. designed the experiments and analyzed the data. Y.W., N.X.N., W.Z., Y.Y., and X.B. generated key materials and executed the experiments. N.X.N., Y.W., and Y.J. wrote the manuscript with input from X.B. Y.J. supervised the project and revised the manuscript.

Declaration of interests: The authors declare no competing interests.

Graphical Abstract

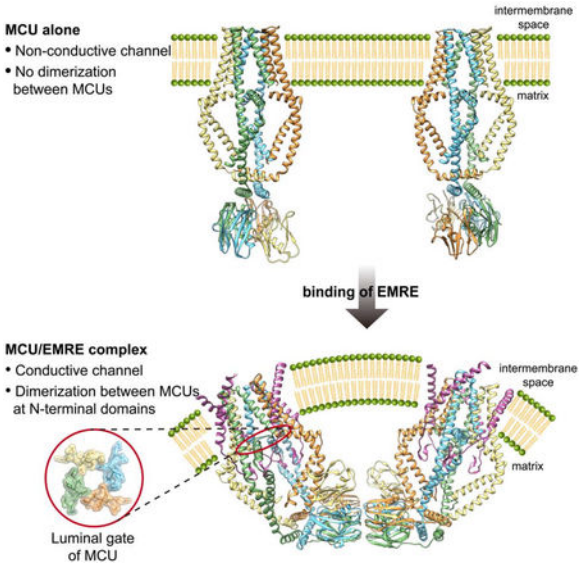

Keywords

intracellular calcium signaling; calcium channel; mitochondrial calcium uniporter

Introduction

It has long been appreciated that mitochondria regulate intracellular calcium signaling and, as a result, an array of physiological processes ranging from metabolism to cell death (Berridge, 2003; Rizzuto, 2012). Although early studies revealed that mitochondrial calcium uptake is mediated by a highly selective calcium channel that is localized to the inner mitochondrial membrane (IMM) called the mitochondrial calcium uniporter (MCU) (Gunter, 1990; Kirichok, 2004), the precise mechanism underlying MCU's function still remains poorly understood. In humans, the MCU is a protein complex consisting of at least four components: MCU (Baughman, 2011; De Stefani, 2011), the ion transport component; EMRE (Sancak, 2013), an essential MCU regulator; and MICU1 (Perocchi, 2010) and MICU2 (Plovanich, 2013), which function as calcium sensing, gate-keepers of the uniporter. As a complex, EMRE not only confers function to MCU but also mediates the physical interaction between MICU1 and MICU2 with the channel component (Tsai, 2016), which set the threshold at which mitochondrial calcium uptake can occur (Kamer, 2014; Patron, 2014).

Although MCU is found in all major eukaryotic taxa, EMRE is a metazoan-specific, single membrane-spanning protein that functions as an essential accessory subunit of MCU among these organisms (Bick, 2012; Sancak, 2013). Interestingly, MCU from fungi and *Dictyostelium discoideum*, whose genomes lack EMRE, can also mediate mitochondrial calcium uptake (Kovacs-Bogdan, 2014; Song, 2016). Thus, it remains unclear why EMRE is required for MCU's function among higher eukaryotes. EMRE's physiological significance,

however, has been demonstrated in vitro and in vivo. The identification of the first human genetic mutation linked to the uniporter highlights the role of abnormal mitochondrial calcium handling in the development of neuromuscular disease (Logan, 2014), with subsequent studies in mice showing that the resulting mitochondrial calcium overload can be attenuated through the modulation of EMRE expression (Liu, 2016).

Recently, several fungal MCU structures were reported (Baradaran, 2018; Fan, 2018; Nguyen, 2018; Yoo, 2018), revealing the architectural arrangement of the pore-forming component of the uniporter and MCU's potential mechanism for Ca^{2+} selectivity and transport. However, it remains unclear how representative these structures are with respect to their metazoan counterparts, since it has been shown that fungal mitochondrial calcium uptake is different from that of metazoans (Carafoli, 1971). Here, we present the cryo-EM structure of human MCU in complex with EMRE (HsMCU/EMRE), revealing a tetrameric channel with notable features that are distinct from those of fungal MCU. Structural and functional analysis also led us to pinpoint the juxtamembrane loop – a stretch of six residues in human MCU – as well as the extended linker of EMRE as the crucial elements that mediate the channel's dependence on EMRE for function among metazoan mitochondrial calcium uniporters.

Results

Unique architecture of the human MCU/EMRE complex

The human MCU/EMRE complex was purified and reconstituted into nanodiscs (Figure 1A and 1B) (Denisov, 2004), and its structure was determined by phase-plate cryo-EM to a resolution of 3.6 Å, using the gold-standard Fourier shell correlation (FSC) = 0.143 criteria (Figures S1; STAR Methods). The cryo-EM density maps were of sufficient quality for model building of major parts of the protein complex (Figure S1G and S1H). Additionally, we reconstituted the purified protein into liposomes for calcium uptake measurements, recapitulating known properties of the uniporter such as voltage-dependent Ca^{2+} uptake and inhibition by Ru360 (Figures 1C and 1D; STAR Methods).

Although human MCU (HsMCU) assembles as a tetramer like its fungal counterparts (Baradaran, 2018; Fan, 2018; Nguyen, 2018; Yoo, 2018), their structures differ quite significantly. For instance, each HsMCU subunit can be segmented into four structural domains, as opposed to three for fungal MCU: the N-terminal domain (NTD), linker helix domain (LHD) – which is absent in fungal MCU, coiled-coil domain (CCD), and transmembrane domain (TMD) (Figures 2A, 2B and S2). Four EMRE subunits – each sitting on the periphery of the transmembrane pore – interact with an MCU tetramer, which defines the stoichiometry of MCU subunits to EMRE as one to one (Figure 2A; Movie S1). EMRE consists of two structural elements: a transmembrane helix (TM0) that packs at a 45° angle against TM1 of one MCU subunit and an N-terminal β-hairpin that sits snugly within a groove created by CC2a and CC2b of a neighboring MCU subunit (Figures 2A and 2B; Figure S2).

Overall, the TMD and CCD of HsMCU resemble that of our previously determined cryo-EM structure of MCU from the fungus *N. fischeri* or NfMCU (Nguyen, 2018), with the

notable exception that the CCD is more outwardly bulged, generating significantly larger fenestrations (Figure S3A). Additionally, HsMCU contains an LHD that appears to segment the highly conserved pore domain from the less conserved NTD of MCU (Figure 2B). Although the TMD and CCD of HsMCU is four-fold symmetric, symmetry breakdown occurs at the LHD and NTD (Figures 2A–2C). Most strikingly, the four NTDs assemble in a side-by-side configuration to form an arc that swings to one side of the channel (Figure 2C) – as was also observed in the low resolution cryo-EM structure of zebrafish MCU (Baradaran, 2018) – rather than the enclosed tetrameric ring seen among fungal MCUs (Baradaran, 2018; Fan, 2018; Nguyen, 2018; Yoo, 2018) (Figure S3B).

The unusual arrangement of the NTD tetramer dictates that each NTD and its respective CC1 differ in their connectivity and orientation (Figures 2B and 2D). Consequently, the helical length and range of each linker helix, as well as its orientation, vary among the four subunits (Figures 2B, 2D, 2E and S2). The linker helix from opposing MCU subunits dimerizes in an antiparallel fashion – each pair stacking on top of the other – to assemble into a helical bundle that stacks perpendicularly with respect to the channel axis (Figure 2E). The presence of the linker helix in HsMCU makes the unusual oligomerization of the NTD possible and appears to be metazoan-specific as it was not observed in fungal MCU (Baradaran, 2018; Fan, 2018; Nguyen, 2018; Yoo, 2018) (Figure S2).

NTD mediated dimerization of HsMCU

Unexpectedly, two MCU channels form a v-shaped dimer through extensive dimerization interactions at the NTD (Figure 3A; Movie S2). While the individual NTD of HsMCU resembles that of the previously determined crystal structures (Lee, 2016; Lee, 2015) – a barrel consisting of seven β-strands (β1–7) and two α-helices (α1 and α2) that seals off the side and top of the barrel, respectively (Figure 3B) – its oligomerization is unique among tetrameric cation channels whose structures have been determined to date (Figures 3C and 3D). Within each channel, four NTDs from each subunit assemble along the same longitudinal axis primarily through hydrogen bonding between main chain atoms on β5 of one subunit and β3 of a neighboring subunit (Figure 3C). The NTD further mediates the oligomerization of two MCU channels through multiple sets of salt bridges and hydrogen bonds at the dimerization interface, wherein the outermost NTD from each channel are excluded (Figures 3A and 3D). Specifically, D123 on the NTD of one channel forms electrostatic interactions with arginines on the NTD of the opposing channel (Figure 3D).

As expected, a charge swap mutation of D123R abolished dimerization of HsMCU (Figures S4A–S4C). Interestingly, neither the D123R mutation nor deletion of the entire NTD altered calcium uptake (Figures S4D–S4F). Thus, the NTD appears to be functionally dispensable in the context of our in vitro mitochondrial Ca^{2+} uptake assay. However, we believe MCU's NTD and its unique oligomerization warrants further investigation because post-translational modifications (PTMs) to the NTD of MCU and their pathophysiological implications have been reported. Phosphorylation of two serine residues – S57 and S92 – in the NTD of MCU by the Ca^{2+}/calmodulin-dependent protein kinase II (CaMKII) has been shown to increase MCU current, which promotes the opening of the permeability transition pore and myocardial cell death in mouse models (Joiner, 2012). Additionally, a highly conserved

cysteine – C97 in human MCU – was recently shown to undergo S-glutathionylation and functions as a reactive oxygen species (mROS) sensor in the mitochondrial matrix; oxidation or mutation of C97 resulted in elevated mitochondrial Ca^{2+} and mROS accumulation, leading to calcium overload-induced cell death (Dong, 2017). It is worth noting that the PTMs that have been identified thus far all map to the vicinity of the dimerization interface, suggesting that this unique locus in MCU may function as a regulatory hotspot.

The pore of HsMCU

The evolutionary diversity of the mitochondrial calcium uniporter (Bick, 2012) along with its functional differences among eukaryotic taxa (Carafoli, 1971; Huang, 2018; Kovacs-Bogdan, 2014) have raised the possibility that metazoan MCUs may be structurally different than their fungal counterpart. However, structure analysis of the HsMCU pore, which consists of the CCD and TMD, shows notable similarities between human and fungal MCU.

The CCD of HsMCU consists of three helices: CC1, CC2a and CC2b (Figure 4A). CC1 is an exceptionally long alpha helix with an exaggerated bend in the vicinity of P216 and is contiguous with TM1 (Figures 4A). The second coiled-coil of HsMCU is broken into two halves, with CC2a and CC2b adopting an L-shaped configuration to interact with the C- and N-terminal halves of CC1, respectively (Figures 2B and 4A). Notably, a juxtamembrane loop (JML) connecting CC2a and TM2, which was disordered in the previously determined structures of fungal MCU (Baradaran, 2018; Fan, 2018; Nguyen, 2018; Yoo, 2018), is clearly defined in HsMCU – running parallel to the lipid bilayer to seal off the base of the TMD (Figures 2B and 4).

The ion conduction pore of HsMCU is nearly identical to that of NfMCU (Figures 4A to 4E). The pore forming TM2 helix interacts extensively with TM1 of a neighboring subunit but not that of the same subunit, thereby creating a wide gap between TM1 and TM2 within each subunit, which would be sealed off by lipids (Figure 4A). With the juxtamembrane loop well-resolved in the structure of HsMCU, we observe two constriction points at opposite ends of the ion conduction pathway (Figures 4B and 4C). The first constriction occurs at E264 of the $_{260}$WDIMEP$_{265}$ selectivity filter sequence (Figure 4D). Four E264 residues in a channel tetramer form the narrowest part of the filter with their side chain carboxylates directly coordinating a Ca^{2+}, generating a high affinity Ca^{2+} binding site analogous to the EEEE locus of voltage-gated Ca^{2+} channels (Ca_V). Four D261 residues encircle the cytosolic pore entrance of MCU with a wider diameter and likely form a low affinity site for a hydrated Ca^{2+} (Figures 4B to 4D). As was proposed for NfMCU (Nguyen, 2018), the proximity of the two rings of acidic residues within the selectivity filter of HsMCU suggests a two-site, single file pore for selective Ca^{2+} permeation, which is conceptually similar to the classical ion conduction model for Ca_V channels (Almers, 1984; Hess, 1984; Yang, 1993).

As was also previously described in fungal MCU (Baradaran, 2018; Fan, 2018; Nguyen, 2018; Yoo, 2018), the highly conserved W260 and P265 flanking the DIME motif also contribute to the structural integrity of the selectivity filter in human MCU. First, the phenyl ring of W260 forms CH/π interactions with P265 of a neighboring subunit in a stacked-like configuration. Second, the amino group of the pyrrole ring forms intra- and intermolecular

hydrogen bonds with the carboxylate oxygen of E264, stabilizing its side chain in a conformation that is optimal for high-affinity Ca^{2+} binding (Figure 4D). In fungal and human MCU, replacing the equivalent Trp or Pro with alanine resulted in a functionally dead channel (Baradaran, 2018; Fan, 2018; Nguyen, 2018). Thus, the ion selectivity filter of HsMCU is tightly packed and conformationally rigid.

The second constriction point in the HsMCU pore occurs at the juxtamembrane loop, a stretch of six well-ordered residues that connect CC2a and TM2 (Figures 4B, 4C and 4E). Residues E288 and V290 from each JML encircle the pore exit to produce an opening measuring ~9 Å in diameter, wide enough for Ca^{2+} to exit and enter into bulk solvent. We predict that the JML in HsMCU functions as the luminal gate among metazoan MCUs and requires EMRE to maintain it in an open conformation; thus, modification of the JML in HsMCU may uncouple MCU's dependence on EMRE for channel activity. Since MCU from *D. discoideum* and *N. fischeri* have been shown to function independently of EMRE (Kovacs-Bogdan, 2014; Nguyen, 2018), we asked whether swapping their JML with that of HsMCU can restore activity to the latter. Indeed, the JML from either *D. discoideum* or *N. fischeri* is sufficient to confer mitochondrial calcium uptake to HsMCU in the absence of EMRE while HsMCU containing the JML from *Drosophila* still requires EMRE to function (Figures 4F and S5). Thus, metazoan MCU maintains a luminal gate at the JML that requires EMRE to remain open.

EMRE and its interactions with MCU

Biochemical analyses of the MCU complex has led to conflicting proposals on the orientation of EMRE and how it interacts with MCU (Tsai, 2016; Vais, 2016). The structure of the HsMCU/EMRE complex resolves this conflict, showing that EMRE is a single transmembrane protein with its N-terminus facing the mitochondrial matrix (Figures 1A and 1B). Excluding the mitochondrial targeting sequence (MTS), the first 17 residues on the N-terminus and the last 10 residues on the C-terminus – containing the C-terminal acidic domain proposed to interact with MICU1 – are disordered in our structure (Figure S2). The single membrane spanning helix of EMRE is attached to the periphery of MCU (Figure 2A), while the N-terminal β-hairpin connects to the TM0 of EMRE via an extended loop (Figure 2B), which appears to adopt a rigid structure and contains two highly conserved prolines (Figure S2B).

EMRE makes three major points of contact with MCU, extended across two neighboring MCU subunits (Figure 5A). First, the central part of its TM0 helix forms extensive hydrophobic contacts with TM1 of MCU (Figure 5B). Several key interfacial residues between the two TMs were previously defined by scanning mutagenesis and confirmed by our structure (Tsai, 2016). Second, the N-terminus of TM0 forms hydrophobic contact with the C-terminus of TM2 from the neighboring MCU subunit (Figure 5C). Third, the N-terminal β-hairpin of EMRE, along with the extended loop containing the highly conserved $_{58}PKP_{60}$ sequence, interact with CC2 of a neighboring MCU subunit mainly through van der Waals interactions (Figure 5D). Notably, the extended side chain of R297 on CC2a connects the JML of MCU to EMRE by forming hydrogen bonds with the hydroxyl group of T285 (on the JML of MCU) and the backbone carbonyl of V61 on EMRE (Figure 5C).

Mechanism of EMRE-dependent gating in metazoan MCU

Phylogenetic analysis of the mitochondrial calcium uniporter shows that EMRE is a recent innovation – specific only to metazoans – while the pore component, MCU, probably existed in the earliest mitochondria (Sancak, 2013). Thus, in acquiring EMRE, MCU somehow lost the ability to function on its own – raising the question: What is the mechanism by which EMRE regulates the ion conductivity of MCU? To address this question, we sought to determine the structure of human MCU alone. However, without EMRE, HsMCU was poorly expressed and unstable as it was prone to aggregate throughout purification. Nevertheless, a sufficient amount of HsMCU alone was obtained and reconstituted into nanodiscs, and its structure was determined to 7.7 Å (Figure 6A and Figure S6).

Despite the low resolution, several notable differences are observed in the HsMCU alone structure as compared to the HsMCU/EMRE complex. The CCD becomes less outwardly bulged in the absence of EMRE – a consequence of the concerted movement of the CC1 and CC2 helices toward the central axis (Figure 6). The greatest conformational displacement within the CCD occurred in the vicinity where the β-hairpin and extended linker of EMRE interacts with the CCD of MCU. We suspect that the N-terminal region of EMRE, which consists of the β-hairpin and extended linker, may function like a hook, pulling CC2a away from the central axis and dragging along with it CC1 and CC2b. Notably, the extended linker of EMRE contains a highly conserved $_{58}$PKP$_{60}$ motif that appears to limit the flexibility of both the extended linker and β-hairpin (Figures 5D and S2B). In other words, the rigid nature of Pro allows the PKP motif to function as a molecular clamp that locks the luminal soluble domain of EMRE into the fenestrations at the CCD of MCU. As the luminal gate-forming JML is tightly tethered to CC2a, EMRE's β-hairpin and extended linker likely stabilize the luminal gate of MCU in the open conformation.

Although the gate-forming JML region was poorly resolved in the HsMCU alone structure, we envision that, in the absence of EMRE, the movement of CC2a toward the central axis would induce a similar concerted movement in the JML as well, which would result in a narrowing of the pore exit (Figure 6B and 6C). Interestingly, serial truncation of human EMRE shows that, while the β-hairpin is dispensable, the extended linker is crucial, for regulating the conductivity of MCU (Figure 5E). In fact, we can remove much of the N-terminus of EMRE – up to the start of the extended linker (K59) – and observe a progressive reduction in Ca^{2+} uptake, with further deletions resulting in no EMRE expression. Indeed, it has been shown that a single point mutation (P60A) in the $_{58}$PKP$_{60}$ motif of the extended linker of mouse EMRE is sufficient to abolish mitochondrial calcium uptake (Yamamoto, 2016). We suspect that this mutation removes the rigidity of the extended linker and changes its conformation, thus uncoupling EMRE from MCU.

In the absence of EMRE, the NTDs of HsMCU swing downward, resulting in a semi-circular ring that sits at the base rather than to the side of the channel, as was previously observed in the low resolution structure of zebrafish MCU (Baradaran, 2018). The conformational change in the NTDs likely resulted from the inward translation of the CC1 helices toward the central axis and the clockwise rotation of the helical bundle that constitutes the linker helices (Figure 6B). Consequently, the HsMCU channel becomes monomeric in the absence of EMRE, as demonstrated both biochemically and structurally

(Figure S6). Thus, in addition to maintaining MCU in an open, conductive state through direct regulation of the luminal channel gate at the JML, EMRE also plays a role in mediating the dimerization of the MCU/EMRE complex. Given the poorly resolved density for the NTDs as compared to the rest of the HsMCU structure, we also suspect that the NTD of MCU is conformationally dynamic in the absence of EMRE.

Discussion

Our functional and structural data on the human MCU/EMRE complex firmly establish that MCU is a tetrameric calcium channel with a conserved pore architecture similar to its fungal counterparts (Baradaran, 2018; Fan, 2018; Nguyen, 2018; Yoo, 2018). We also define the structure of EMRE for the first time, showing its stoichiometry and orientation with respect to MCU as well as atomic details of their interactions. The structure also led us to pinpoint the juxtamembrane loop of MCU as the luminal gate, whose opening among metazoan MCUs requires EMRE. Furthermore, we identify the extended linker of EMRE as the critical element for the EMRE-dependent regulation of metazoan MCU.

A distinct feature of human MCU when in complex with EMRE is that its NTD adopts a unique oligomeric assembly, whereby four NTDs pack in a side-by-side configuration to mediate the dimerization of two MCU/EMRE complexes. While removal of the NTD does not seem to affect mitochondrial Ca^{2+} uptake (Figure S8), recent studies, however, suggest that the NTD plays an important role in modulating the function of MCU under conditions of cellular stress (Dong, 2017; Joiner, 2012; Lee, 2016). Thus, the structure of the MCU/EMRE complex will serve as a crucial template for future studies aimed at dissecting the regulatory mechanisms governing mitochondrial Ca^{2+} uptake.

It has long been noted that efficient mitochondrial calcium uptake requires mitochondria to be proximal to the endo-/sarcoplasmic reticulum (ER/SR), where microdomains of micromolar Ca^{2+} concentrations are produced (Rizzuto, 1993, 1998). This, in turn, allows the gate-keeping proteins, MICU1 and MICU2, to disinhibit MCU, allowing for Ca^{2+} entry into the mitochondrial matrix (Kamer, 2014; Patron, 2014). Altering the expression of MICU1 has been shown to cause mitochondrial Ca^{2+} overload in cells (Mallilankaraman, 2012), mice (Liu, 2016), and humans (Logan, 2014). Given the tubular structure of the mitochondrial cristae and the low calcium binding affinity of MICU1 and MICU2, it makes intuitive sense for MCU to be localized to regions on the inner mitochondrial membrane (IMM) that are most proximal to the outer mitochondrial membrane (OMM), thus conferring greater sensitivity of MCU to elevations in cytoplasmic Ca^{2+} concentrations. We suspect that the unique dimeric assembly of two MCU/EMRE complexes may play a role in the regulation of mitochondrial Ca^{2+} uptake through the localization of MCU to specific regions within the cristae membrane – preferentially to the curved membrane regions. On the premise of membrane curvature requirement, we speculate that the EMRE-dependent dimerization of MCU would promote the channel to be localized to the inner boundary membrane instead of invaginated regions of the cristae, and, thereby, may play a role in the regulation of mitochondrial Ca^{2+} uptake through the localization of MCU to specific regions within the inner membrane. Given that the post-translational modifications to MCU that have been identified thus far all localize to the vicinity of the dimeric interface, the structure

of the human MCU/EMRE complex will serve as a crucial template for further investigation into the physiological and cellular relevance of the dimerization of the MCU/EMRE complex.

STAR Methods

EXPERIMENTAL MODEL AND SUBJECT DETAILS

Cell Lines—HEK293F cells (Thermo Fisher Scientific) were maintained in FreeStyle 293 Expression Media (Thermo Fisher Scientific) at 37 °C, 8% CO_2, 130 rpm in a Reach-In CO_2 Incubator (Thermo Fisher Scientific) throughout. HEK293 cells (ATCC) and MCU knockout ($MCU^{-/-}$), EMRE knockout ($EMRE^{-/-}$) or MCU/EMRE double knockout ($MCU^{-/-}$/$EMRE^{-/-}$) HEK293 cells (Tsai, 2016) – used for electrophysiology and mitochondrial calcium uptake assays, respectively – were grown in DMEM media (Thermo Fisher Scientific) supplemented with 10% fetal bovine serum (FBS, Thermo Fisher Scientific) and kept in a 37°C, 5% CO_2 incubator. All cell lines are female in origin.

METHOD DETAILS

Expression of the MCU/EMRE complex—For heterologous expression of the MCU/EMRE complex, full-length human copies of MCU (NCBI: NM_138357.2), EMRE (NCBI: NM_033318.4), and MICU1 (NCBI: NM_001195518.1) were amplified by PCR from human cDNA clones (purchased from the McDermott Center, UT Southwestern Medical Center) and then sub-cloned into pEZT-BM vectors (Morales-Perez, 2016) containing a C-terminal Strep-tag (MCU and EMRE) or C-terminal Flag-tag (MICU1).

The sequence for the C-terminal Strep-tag HsMCU (MCU_{cStrep}) is:
MAAAAGRSLLLLLSSRGGGGGGAGGCGALTAGCFPGLGVSRHRQQQHHRTVHQRI
AS
WQNLGAVYCSTVVPSDDVTVVYQNGLPVISVRLPSRRERCQFTLKPISDSVGVFLRQ
LQ
EEDRGIDRVAIYSPDGVRVAASTGIDLLLLDDFKLVINDLTYHVRPPKRDLLSHENAA
TLNDVKTLVQQLYTTLCIEQHQLNKERELIERLEDLKEQLAPLEKVRIEISRKAEKRT
TLVL
WGGLAYMATQFGILARLTWWEYSWDIMEPVTYFITYGSAMAMYAYFVMTRQEYV
YP
EARDRQYLLFFHKGAKKSRFDLEKYNQLKDAIAQAEMDLKRLRDPLQVHLPLRQIG
EK DWSHPQFEK

The sequence for C-terminal Strep-tag HsEMRE ($EMRE_{cStrep}$) is as follows:
MASGAARWLVLAPVRSGALRSGPSLRKDGDVSAAWSGSGRSLVPSRSVIVTRSGAIL
PK PVKMSFGLLRVFSIVIPFLYVGTLISKNFAALLEEHDIFVPEDDDDDDWSHPQFEK

The sequence for the C-terminal Flag-tag HsMICU1 ($MICU1_{cFlag}$) is as follows:
MFRLNSLSALAELAVGSRWYHGGSQPIQIRRRLMMVAFLGASAVTASTGLLWKRAH
AE
SPPCVDNLKSDIGDKGKNKDEGDVCNHEKKTADLAPHPEEKKKKRSGFRDRKVME
YE

NRIRAYSTPDKIFRYFATLKVISEPGEAEVFMTPEDFVRSITPNEKQPEHLGLDQYIIKR FD
GKKISQEREKFADEGSIFYTLGECGLISFSDYIFLTTVLSTPQRNFEIAFKMFDLNGDG EV
DMEEFEQVQSIIRSQTSMGMRHRDRPTTGNTLKSGLCSALTTYFFGADLKGKLTIKN FLE
FQRKLQHDVLKLEFERHDPVDGRITERQFGGMLLAYSGVQSKKLTAMQRQLKKHF KEG
KGLTFQEVENFFTFLKNINDVDTALSFYHMAGASLDKVTMQQVARTVAKVELSDHV CD
VVFALFDCDGNGELSNKEFVSIMKQRLMRGLEKPKDMGFTRLMQAMWKCAQETA WD FALPKQ<u>DYKDDDDK</u>

The affinity tags for each construct listed above are underlined. All plasmids were generated following standard protocols using either *E. coli* TOP10 or DH5α (Thermo Fisher Scientific). All mutants were generated using the Quikchange Site-Directed Mutagenesis Kit (Agilent) and confirmed by DNA sequencing.

E. coli DH10bac (Thermo Fisher Scientific) were used to synthesize bacmids, which were subsequently used for the production of baculovirus in *Sf9* cells using Cellfectin II reagent (Thermo Fisher Scientific) following the manufacturer's protocol.

To express the MCU/EMRE/MICU1 complex, HEK293F cells were grown to a density of 3×10^6 cells mL^{-1} in FreeStyle 293 Expression Media (Thermo Fisher Scientific) and then incubated with baculoviruses for MCU_{cStrep}, $EMRE_{cStrep}$, and $MICU1_{cFlag}$ at a ratio of 1:40 (virus:cell) for each virus and 10 mM sodium butyrate. To express MCU alone, only baculoviruses for MCU_{cStrep} and 10 mM sodium butyrate were added to the cell culture. The cells were grown for 48 hours and then harvested by centrifugation at 4000 rpm for 15 minutes.

Purification of the MCU/EMRE complex—To purify the MCU/EMRE/MICU1 complex, the pelleted HEK293F cells were re-suspended in Buffer A (50 mM Tris pH 8.0, 150 mM NaCl), supplemented with protease inhibitors (1 μg/mL each of DNase I, pepstatin, leupeptin and aprotinin, and 1 mM PMSF), and then homogenized by sonication. The protein was extracted by addition of 2% (w:v) n-dodecyl-β-D-maltopyranoside (DDM, Anatrace) supplemented with 0.2% (w:v) cholesteryl hemisuccinate (CHS, Sigma Aldrich) to the cell lysate and then stirred at 4°C for 2 hours. Insoluble components were removed by centrifugation at 40,000 × g, 4°C, 30 minutes and the clarified lysate was then loaded onto a disposable gravity column (BioRad) containing Strep-Tactin sepharose resin (IBA Lifesciences) that was pre-equilibrated with Buffer B (Buffer A + 0.1% DDM, 0.02% CHS). After washing the column with 10 column volumes (CV) of Buffer B, the proteins were eluted with 4 CV of Buffer C (Buffer B + 10 mM desthiobiotin (Sigma Aldrich)). The eluted protein was further purified by size exclusion chromatography using a Superose 6 Increase 10/300 GL column (GE Healthcare) pre-equilibrated with Buffer D (50mM Tris pH 8.0, 150mM NaCl, 0.05% DDM, 0.01% CHS). The main peak – eluting around 14mL – was then collected for further biochemical and structural analysis. In our hands, MICU1 does not

form a stable complex with MCU/EMRE; therefore, following size exclusion purification, only the MCU/EMRE complex can be recovered (Figure 1A and 1B). It has been reported that MICU1 interacts with MCU through electrostatic interactions with the C-terminal acidic domain (CAD) of EMRE (Tsai, 2016), and we suspect that our current purification conditions may be too harsh to maintain this delicate interaction between MICU1 and EMRE. The same procedure was used for the purification of MCU alone.

Reconstitution of MCU/EMRE into nanodiscs—The detergent solubilized MCU/EMRE complex was reconstituted into nanodisc (Denisov, 2004) by combining the following components to a molar ratio of 1:4:10 (MCU/EMRE: MSP1: lipids (POPC:POPE:POPG, 3:1:1 molar ratio)). To remove detergents from the reaction, 0.4 g of BioBeads (BioRad) was added to the reaction and incubated with gentle agitation at 4 °C for 6 hours. BioBeads were replaced two additional times before the sample was further purified by gel filtration using a Superose 6 Increase 10/300 GL column (GE Healthcare) pre-equilibrated with Buffer A. The main peak – eluting around 14mL (Extended Data Fig. 3a and b) – was collected, concentrated to 1.3 mg/mL using an Amicon centrifugal concentrator (100kD cut-off, Millipore), and immediately used for cryo-EM grid preparation. The same procedure was used for the reconstitution of MCU alone into nanodiscs.

Cryo-EM data acquisition—The cryo-EM grids were prepared by applying 3 μL of the MCU/EMRE-nanodisc complex to a glow-discharged Quantifoil R1.2/1.3 300-mesh gold holey carbon grid (Quantifoil, Micro Tools GmbH, Germany) and blotted for 4.0 seconds under 100% humidity at 4 °C before being plunged into liquid ethane using a Mark IV Vitrobot (FEI). Micrographs were acquired on a Titan Krios microscope (FEI) operated at 300 kV with a K2 Summit direct electron detector (Gatan), using a slit width of 20 eV on a GIF-Quantum energy filter and a Volta phase plate (Danev, 2016, 2017). EPU software (FEI) was used for automated data collection following standard FEI procedure. A calibrated magnification of 59,523x was used for imaging, yielding a pixel size of 0.84 Å on images. The defocus was set at −0.5 μm. Each micrograph was dose-fractionated to 30 frames under a dose rate of 4 e^{-}/pixel/s, with a total exposure time of 12 s, resulting in a total dose of about 60 $e^{-}/Å^2$.

For the MCU-nanodisc sample, micrographs were acquired using a slit width of 20 eV on a GIF-Quantum energy. A calibrated magnification of 46,729x was used for imaging, yielding a pixel size of 1.07 Å on images. Each micrograph was dose-fractionated to 30 frames under a dose rate of 5 e^{-}/pixel/s, with a total exposure time of 15 s.

Image processing—Motion correction was performed on the MCU/EMRE-nanodisc dataset (1,653 movie stacks) using the MotionCorr2 program (Zheng, 2017) and the CTF parameters of the micrographs were estimated using the GCTF program (Zhang, 2016). All other steps of image processing were performed using RELION2.1 (Scheres, 2012). Initially, about 1,000 particles were manually picked from a few micrographs. Class averages representing projections of HsMCU/EMRE in different orientations were selected from the 2D classification of the manually picked particles, and used as templates for automated particle picking from the full dataset of 1,491 micrographs. The 372,552 extracted particles were binned 3 times and subjected to 2D classification, and a total of 64,418 particles were

finally selected for 3D classification using the initial model generated by RELION as the reference. Two of the 3D classes showed good secondary structural features and their particles were selected, combined and re-extracted into the original pixel size of 0.84 Å. After 3D refinement without any symmetry imposed and particle polishing, the resulting 3D reconstructions from 30,979 particles yielded an EM map at 3.8 Å resolution. Further 3D classification suggested swinging motions of two neighboring channel complexes. To improve the resolution, we performed symmetry expansion and focused refinement as described previously (Bai, 2015; Nguyen, 2016; Zhou, 2015). To do so, all particles in the dataset were duplicated and rotated by 180° according to the C2 symmetry by using the "relion_particle_symmetry_expand" command. The original and rotated particles were combined to form the symmetry expanded dataset. Subsequently, the density for the transmembrane domain, coiled-coil domain, and linker helix domain of one HsMCU/EMRE complex was subtracted from the particles in the symmetry expanded dataset. The modified particle set was subjected to another round of 3D refinement with a soft mask around one HsMCU/EMRE complex as well as the N-terminal domain from the neighboring complex, leading to a markedly improved resolution of 3.6 Å for the entire HsMCU/EMRE complex. All resolutions were estimated by applying a soft mask around the protein density and the gold-standard Fourier shell correlation (FSC) = 0.143 criterion. ResMap was used to calculate the local resolution map (Kucukelbir, 2014).

For the MCU-nanodisc datasets, the 1,309,952 extracted particles were binned 3 times and subjected to 2D classification, and a total of 427,403 particles were finally selected for 3D classification using the cryo-EM map of zebrafish MCU (EMD-7972) as the initial model. After 3D refinement without any symmetry imposed, the resulting 3D reconstructions from 93,255 particles yielded an EM map at 7.7 Å resolution.

Model building, refinement, and validation—The cryo-EM map of the HsMCU/EMRE complex was of excellent quality (Extended Data Fig. 2), allowing for *de novo* atomic model building using Coot. Since the crystal structure of the NTD of human MCU (Lee, 2015) (PDB: 4XTB) fits nicely in the EM map, it was used as a guide to build the NTD of HsMCU. Although the structure of EMRE is not known, the cryo-EM map shows clear, continuous density for EMRE (Extended Data Fig. 2). Amino acid assignment was achieved based on the clearly defined density for bulky residues (Phe, Trp, Tyr, and Arg). Models were refined against summed maps using phenix.real_space_refine, with secondary structure restraints applied (Adams, 2010). The model was validated using previously described methods to avoid overfitting (Amunts, 2014; DiMaio, 2013). The 3.6 Å EM density map of HsMCU/EMRE allowed us to construct a model containing the following residues for MCU: chain A, 74–346, chain C: 74–341, chain E: 74–343 and chain G: 75–164, 177–336; EMRE: chain B: 48–96, chain D: 48–96, chain F 48–96, chain H: 48–95. To build a model of the dimer of the MCU/EMRE complex, the single MCU/EMRE complex model was fitted into the 3.8 Å EM map containing the dimer of the HsMCU/EMRE complex and then manually adjusted in Coot (Emsley, 2010). The statistics for the model's geometries, summarized in Table S1, were generated using MolProbity (Chen, 2010). Pore radii were calculated using the HOLE program (Smart, 1996). The model for the MCU structure in the absence of EMRE was generated by fitting the TMD, CCD, LHD and NTD

from the MCU/EMRE complex structure into the cryo-EM map of HsMCU alone using rigid body movement in COOT (Emsley, 2010). All the figures were prepared in PyMol (Schrödinger, 2015) or Chimera (Pettersen, 2005).

Radioactive $^{45}Ca^{2+}$ flux assay—The purified HsMCU/EMRE complex was reconstituted into liposomes following the same protocol as previously described for the reconstitution of NfMCU (Nguyen, 2018) with slight modifications. Detergent solubilized HsMCU/EMRE was incubated with a lipid mixture consisting of 3POPC: 1POPE: 1POPG (molar ratio) in dialysis buffer (50 mM HEPES pH=7.4, 150 mM KCl) to a final molar ratio of 1:500 (MCU/EMRE: lipids) with gentle agitation at 4 °C for 1 hour and then dialyzed (using dialysis tubing with a molecular weight cutoff of 12,000–14,000 Da, Spectra/Por) against 1L of dialysis buffer at 4°C to remove detergent. Fresh dialysis buffer (1L each time) was exchanged every 18–20 hours for a total of 3 exchanges. Following dialysis, the HsMCU/EMRE proteoliposomes were divided into 100μL aliquots, flash frozen in liquid nitrogen, and stored at −80°C. For all flux assays, three separate batches of HEK293F cells were grown to express the HsMCU/EMRE/MICU1 complex. The protein was then purified individually and used immediately for reconstitution into liposomes. Radioactive $^{45}Ca^{2+}$ flux assay was performed as previously described for NfMCU (Nguyen, 2018).

Mitochondrial calcium uptake assay—As specified in the figure legend, mitochondrial calcium uptake was performed on MCU knockout ($MCU^{-/-}$), EMRE knockout ($EMRE^{-/-}$) or MCU/EMRE double knockout ($MCU^{-/-}/EMRE^{-/-}$) HEK293 cells following a previously described protocol (Tsai, 2016). Briefly, the cells were grown to 90–95% confluency in a 10 cm dish (Corning) and then transfected with 30 μg each of MCU and EMRE plasmids using Lipofectamine 2000 (Thermo Fisher Scientific). Fresh media was replaced 6 hours following transient transfection, and the cells were grown in a 37°C CO_2 incubator for an additional 48 hours.

The transfected cells were harvested by EDTA-trypsin digestion, washed with 5 mL of uptake buffer (20 mM HEPES pH 7.4, 125 mM KCl, 2 mM K_2HPO_4, 1 mM $MgCl_2$, 5 mM glutamate, 5 mM malate, 20 μM EGTA) three times, and then re-suspended in uptake buffer to a final concentration of 15×10^6 cells mL^{-1}. The cells were maintained on ice throughout. To measure calcium uptake, 100 μL of cell suspension were transferred to a 96-well plate (Corning) and the following reagents were added sequentially: 1 μM Oregon Green 488 BAPTA-6F, 0.01% digitonin, and 40 μM $CaCl_2$. Calcium uptake was monitored in a Molecular Devices SpectraMax M3 plate reader (excitation/emission: 485nm/535nm) for 5 minutes.

To ensure protein expression was comparable among the MCU and EMRE mutants tested in our uptake assay, western blot analysis was performed on each sample used for each experiment. Mouse anti-human MCU antibodies (Abcam) and mouse anti-Strep antibodies (GenScript) were used to detect MCU and EMRE, respectively. Mouse anti-β-actin (Santa Cruz Biotechnology) was used as a loading control. HRP-conjugated sheep anti-mouse antibodies (GE Healthcare) were used as the secondary antibodies.

Functional assay analysis—All functional data were analyzed in GraphPad Prism 7 (GraphPad Software, Inc.) or OriginPro 8 (OriginLab Corp.). To obtain the rate of calcium uptake, the linear phase of the uptake measurement – the first 25 seconds of the reaction following $CaCl_2$ administration – was determined by fitting the data to a linear regression equation in OriginPro 8; the slope of the fit is taken as the rate of calcium uptake. Further analysis such as normalization are indicated in the figure legend.

QUANTIFICATION AND STATISTICAL ANALYSIS

Cryo-EM—Resolution estimations of cryo-EM density maps are based on the 0.143 Fourier Shell Correlation criterion (Rosenthal, 2003).

DATA AND SOFTWARE AVAILABILITY

Data Resources—Atomic coordinates and maps of the HsMCU/EMRE complex dimer of channel (PDB: 6O58; EMDB: EMD-0625), HsMCU/EMRE complex monomer of channel and neighboring NTD (PDB: 6O58; EMDB: EMD-0626), and the cryo-EM map of HsMCU alone (EMDB: EMD-0627) have been deposited into the Protein Data Bank (http://www.rcsb.org) and Electron Microscopy Data Bank (https://www.ebi.ac.uk/pdbe/emdb/).

Supplementary Material

Refer to Web version on PubMed Central for supplementary material.

Acknowledgments:

Cryo-EM data were collected at the University of Texas Southwestern Medical Center Cryo-EM Facility, which is funded by the CPRIT Core Facility Support Award RP170644; we thank D. Nicastro and D. Stoddard for technical support and facility access. We also thank Drs. C. Miller and M-F. Tsai (HHMI/Brandeis University) for generously providing us with $MCU^{-/-}$, $EMRE^{-/-}$ and $MCU^{-/-}/EMRE^{-/-}$ HEK293 cells and technical assistance with the mitochondrial calcium uptake assay. This work was supported in part by the Howard Hughes Medical Institute (to Y.J.), the National Institutes of Health (grant GM079179 to Y.J.), the Welch Foundation (Grant I-1578 to Y.J.), the Cancer Prevention and Research Initiative of Texas (to X.B.) and the Virginia Murchison Linthicum Scholar in Medical Research fund (to X.B.).

References

Adams P.D.e.a. (2010). PHENIX: a comprehensive Python-based system for macromolecular structure solution. Acta Crystallographica D 66, 213–221.

Almers W, McCleskey EW (1984). Non-selective conductance in calcium channels of frog muscle: calcium selectivity in a single-file pore. J Physiol 353.

Amunts A.e.a. (2014). Structure of the yeast mitochondrial large ribosomal subunit. Science 343, 1485–1489. [PubMed: 24675956]

Bai XC, Rajendra E, Yang G, Shi Y, Scheres SH (2015). Sampling the conformational space of the catalytic subunit of human gamma-secretase. eLife 4, e11182. [PubMed: 26623517]

Baradaran R, Wang C, Siliciano AF, Long SB (2018). Cryo-EM structures of fungal and metazoan mitochondrial calcium uniporters. Nature 559, 580–584. [PubMed: 29995857]

Baughman JM, Perocchi F, Girgis H, Plovanich M, Belcher-Timme CA, Sancak Y, Bao XR, Strittmatter L, Goldberger O, Bogorad RL, et al. (2011). Integrative genomics identifies MCU as an essential component of the mitochodrial calcium uniporter. Nature 476, 341–345. [PubMed: 21685886]

Berridge MJ, Bootman MD, Roderick HL (2003). Calcium signaling: dynamics, homeostasis and remodeling. Nat Rev Mol Cell Biol 4, 517–529. [PubMed: 12838335]

Bick AG, Calvo SE, Mootha VK (2012). Evolutionary diversity of the mitochondrial calcium uniporter. Science 336, 886. [PubMed: 22605770]

Carafoli E, Lehninger AL (1971). A survey of the interaction of calcium ions with mitochondria from different tissues and species. Biochem J 122, 681–690. [PubMed: 5129264]

Chen VB, Arendall WB 3rd, Headd JJ, Keedy DA, Immormino RM, Kapral GJ, Murray LW, Richardson JS, Richardson DC (2010). MolProbity: all-atom structure validation for macromolecular crystallography. Acta Crystallographica D 66, 12–21.

Danev R, Baumeister W (2016). Cryo-EM single particle analysis with the Volta phase plate. eLife 5, e13046. [PubMed: 26949259]

Danev R, Tegunov D, Baumeister W (2017). Using the Volta phase plate with defocus for cryo-EM single particle analysis. eLife 6, e23006. [PubMed: 28109158]

De Stefani D, Raffaello A, Teardo E, Szabo I, Rizzuto R (2011). A forty-kilodalton protein of the inner membrane is the mitochondrial calcium uniporter. Nature 476, 336–340. [PubMed: 21685888]

Denisov IG, Grinkova YV, Lazarides AA, Sligar SG (2004). Directed self-assembly of monodisperse phospholipid bilayer Nanodiscs with controlled size. J Am Chem Soc 126, 3477–3487. [PubMed: 15025475]

DiMaio F, Zhang J, Chiu W, Baker D (2013). Cryo-EM model validation using independent map reconstructions. Protein Sci 22, 865–868. [PubMed: 23592445]

Dong Z, Shanmughapriya S, Tomar D, Siddiqui N, Lynch S, Nemani N, Breves SL, Zhang X, Tripathi A, Palaniappan P, et al. (2017). Mitochondrial Ca2+ Uniporter Is a Mitochondrial Luminal Redox Sensor that Augments MCU Channel Activity. Mol Cell 65, 1014–1028. [PubMed: 28262504]

Emsley P, Lohkamp B, Scott WG & Cowtan K (2010). Features and development of Coot. Acta Crystallographica D 66, 486–501.

Fan C, Fan M, Orlando BJ, Fastman NM, Zhang J, Xu Y, Chambers MG, Xu X, Perry K, Liao M, Feng L (2018). X-ray and cryo-EM structures of the mitochondrial calcium uniporter. Nature 559, 575–579. [PubMed: 29995856]

Gunter TE, Pfeiffer DR (1990). Mechanisms by which mitochondria transport calcium. Am J Physiol 258, C755–786. [PubMed: 2185657]

Hess P, Tsien RW (1984). Mechanism of ion permeation through calcium channels. Nature 301, 453–456.

Huang G, Docampo R (2018). The Mitochondrial Ca2+ Uniporter Complex (MCUC) of Trypanosoma brucei Is a Hetero-oligomer That Contains Novel Subunits Essential for Ca2+ Uptake. MBio 9, e01700–01718. [PubMed: 30228243]

Joiner ML, Koval OM, Li J, He BJ, Allamargot C, Gao Z, Luczak ED, Hall DD, Fink BD, Chen B, Yang J, Moore SA, Scholz TD, Strack S, Mohler PJ, Sivitz WI, Song LS, Anderson ME (2012). CaMKII determines mitochondrial stress responses in heart. Nature 491, 269–273. [PubMed: 23051746]

Kamer KJ, Mootha VK (2014). MICU1 and MICU2 play nonredundant roles in the regulation of the mitochondrial calcium uniporter. EMBO Rep 15, 299–307. [PubMed: 24503055]

Kirichok Y, Krapivinsky G, Clapham DE (2004). The mitochondrial calcium is a highly selective ion channel. Nature 427, 360–364. [PubMed: 14737170]

Kovacs-Bogdan E, Sancak Y, Kamer KJ, Plovanich M, Jambhekar A, Huber RJ, Myre MA, Blower MD, Mootha VK (2014). Reconstitution of the mitochondrial calcium uniporter in yeast. Proc Natl Acad Sci USA 111, 8985–8990. [PubMed: 24889638]

Kucukelbir A, Sigworth FJ & Tagare HD (2014). Quantifying the local resolution of cryo-EM density maps. Nat Methods 11, 63–65. [PubMed: 24213166]

Lee SK, Shanmughapriya S, Mok MCY, Dong Z, Tomar D, Carvalho E, Rajan S, Junop MS, Madesh M, Stathopulos PB (2016). Structural Insights into Mitochondrial Calcium Uniporter Regulation by Divalent Cations. Cell Chem Biol 23, 1157–1169. [PubMed: 27569754]

Lee Y, Min CK, Kim TG, Song HK, Lim Y, Kim D, Shin K, Kang M, Kang JY, Youn H-S, et al. (2015). Structure and function of the N-terminal domain of the human mitochondrial calcium uniporter. EMBO Rep 16, 1318–1333. [PubMed: 26341627]

Liu JC, Liu J, Holmstrom KM, Menazza S, Parks RJ, Fergusson MM, Yu Z-X, Springer DA, Halsey C, Liu C, et al. (2016). MICU1 serves as a molecular gatekeeper to prevent in vivo mitochondrial calcium overload. Cell Rep 16, 1561–1573. [PubMed: 27477272]

Logan CV, Szabadkai G, Sharpe JA, Parry DA, Torelli S, Childs A-M, Kriek M, Phadke R, Johnson CA, Roberts NY, et al. (2014). Loss of function mutations in MICU1 cause a brain and muscle disorder linked to primary alterations in mitochondrial calcium signaling. Nat Genet 46, 188–193. [PubMed: 24336167]

Mallilankaraman K, Doonan P, Cardenas C, Chandramoorthy HC, Muller M, Miller R, Hoffman NE, Gandhirajan RK, Molgo J, Birnbaum MJ, et al. (2012). MICU1 is an essential gatekeeper for MCU-mediated mitochondrial Ca2+ uptake that regulates cell survival. Cell 151, 630–644. [PubMed: 23101630]

Morales-Perez CL, Noviello CM, Hibbs RE (2016). Manipulation of Subunit Stoichiometry in Heteromeric Membrane Proteins. Structure 24, 797–805. [PubMed: 27041595]

Nguyen NX, Armache JP, Lee C, Yang Y, Zeng W, Mootha VK, Cheng Y, Bai XC, Jiang Y (2018). Cryo-EM structure of a fungal mitochondrial calcium uniporter. Nature 559, 570–574. [PubMed: 29995855]

Nguyen THD, Galej WP, Bai XC, Oubridge C, Newman AJ, Scheres SHW, Nagai K (2016). Cryo-EM structure of the yeast U4/U6.U5 tri-snRNP at 3.7 Å resolution. Nature 530, 298–302. [PubMed: 26829225]

Patron M, Checchetto V, Raffaello A, Teardo E, Reane DV, Mantoan M, Granatiero V, Szabo I, De Stefani D, Rizzuto R (2014). MICU1 and MICU2 finely tune the mitochondrial Ca2+ uniporter by exerting opposite effects on MCU activity. Mol Cell 53, 726–737. [PubMed: 24560927]

Perocchi F, Gohil VM, Girgis HS, Bao XR, McCombs JE, Palmer AE, Mootha VK (2010). MICU1 encodes a mitochondrial EF hand protein required for Ca(2+) uptake. Nature 467, 291–296. [PubMed: 20693986]

Pettersen EF, Goddard TD, Huang CC, Couch GS, Greenblatt DM, Meng EC, and Ferrin TE (2005). UCSF Chimera–a visualization system for exploratory research and analysis. J Comput Chem 25, 1605–1612.

Plovanich M, Bogorad RL, Sancak Y, Kamer KJ, Strittmatter L, Li AA, Girgis HS, Kuchimanchi S, De Groot J, Speciner L, et al. (2013). MICU2, a paralog of MICU1, resides within the mitochondrial uniporter complex to regulate calcium handling. PLoS One 8, e55785. [PubMed: 23409044]

Rizzuto R, Brini M, Murgia M, Pozzan T (1993). Microdomains with high Ca2+ close to IP3-sensitive channels that are sensed by neighboring mitochondria. Science 262, 744–747. [PubMed: 8235595]

Rizzuto R, De Stefani D, Raffaello A, Mammucari C (2012). Mitochondria as sensors and regulators of calcium signalling. Nat Rev Mol Cell Biol 13, 566–578. [PubMed: 22850819]

Rizzuto R, Pinton P, Carrington W, Fay FS, Fogarty KE, Lifshitz LM, Tuft RA, Pozzan T (1998). Close contacts with the endoplasmic reticulum as determinants of mitochondrial Ca2+ responses. Science 280, 1763–1766. [PubMed: 9624056]

Rosenthal PB, Henderson R (2003). Optimal determination of particle orientation, absolute hand, and contrast loss in single-particle electron cryomicroscopy. J Mol Biol 333, 721–745. [PubMed: 14568533]

Sancak Y, Markhard A, Kitami T, Kovacs-Bogdan E, Kamer KJ, Udeshi ND, Carr SA, Chaudhuri D, Clapham DE, Li AA, Calvo SE, Goldberger O, Mootha VK (2013). EMRE is an essential component of the mitochondrial calcium uniporter. Science 342, 1379–1382. [PubMed: 24231807]

Scheres SH (2012). RELION: implementation of a Bayesian approach to cryo-EM structure determination. J Struct Biol 180, 519–530. [PubMed: 23000701]

Schrödinger L (2015). The PyMOL Molecular Graphics System, Version 1.8.

Smart OS, Neduvelil JG, Wang X, Wallace BA & Sansom MS (1996). HOLE: a program for the analysis of the pore dimensions of ion channel structural models. J Mol Graph 14, 354–360. [PubMed: 9195488]

Song J, Liu X, Zhai P, Huang J, Lu L (2016). A putative mitochondrial calcium uniporter in A. fumigatus contributes to mitochondrial Ca2+ homeostasis and stress responses. Fungal Genet Biol 94, 15–22. [PubMed: 27378202]

Tsai M-F, Phillips CB, Ranaghan M, Tsai C-W, Wu Y, Willliams C, Miller C (2016). Dual functions of a small regulatory subunit in the mitochondrial calcium uniporter complex. eLife e15545. [PubMed: 27099988]

Vais H, Mallilankaraman K, Mak DD, Hoff H, Payne R, Tanis JE, Foskett JK (2016). EMRE is a matrix Ca2+ sensor that governs gatekeeping of the mitochondrial Ca2+ uniporter. Cell Rep 14, 403–410. [PubMed: 26774479]

Yamamoto T, Yamagoshi R, Harada K, Kawano M, Minami N, Ido Y, Kuwahara K, Fujita A, Ozono M, Watanabe A, Yamada A, Terada H, Shinohara Y (2016). Analysis of the structure and function of EMRE in a yeast expression system. Biochim Biophys Acta 1857, 831–839. [PubMed: 27001609]

Yang J, Ellinor PT, Sather WA, Zhang JF, Tsien RW (1993). Molecular determinants of Ca2+ selectivity and ion permeation in L-type Ca2+ channels. Nature 366, 158–161. [PubMed: 8232554]

Yoo J, Wu M, Yin Y, Herzik MA Jr., Lander GC, Lee SY (2018). Cryo-EM structure of a mitochondrial calcium uniporter. Science 361, 506–511. [PubMed: 29954988]

Zhang K (2016). Gctf: Real-time CTF determination and correction. J Struct Biol 193, 1–12. [PubMed: 26592709]

Zheng SQ, Palovcak E, Armache JP, Verba KA, Cheng Y, Agard DA (2017). MotionCor2: anisotropic correction of beam-induced motion for improved cryo-electron microscopy. Nat Methods 14, 331–332. [PubMed: 28250466]

Zhou M, Li Y, Hu Q, Bai XC, Huang W, Yan C, Scheres SH, Shi Y (2015). Atomic structure of the apoptosome: mechanism of cytochrome c- and dATP-mediated activation of Apaf-1. Genes Dev 29, 2349–2361. [PubMed: 26543158]

Highlights:

- Human MCU is a tetrameric channel with one EMRE bound to each MCU subunit
- EMRE stabilizes the juxtamembrane loop of MCU, conferring EMRE-dependent gating to MCU
- EMRE triggers dimerization of two MCU/EMRE complexes at MCU's N-terminal domains

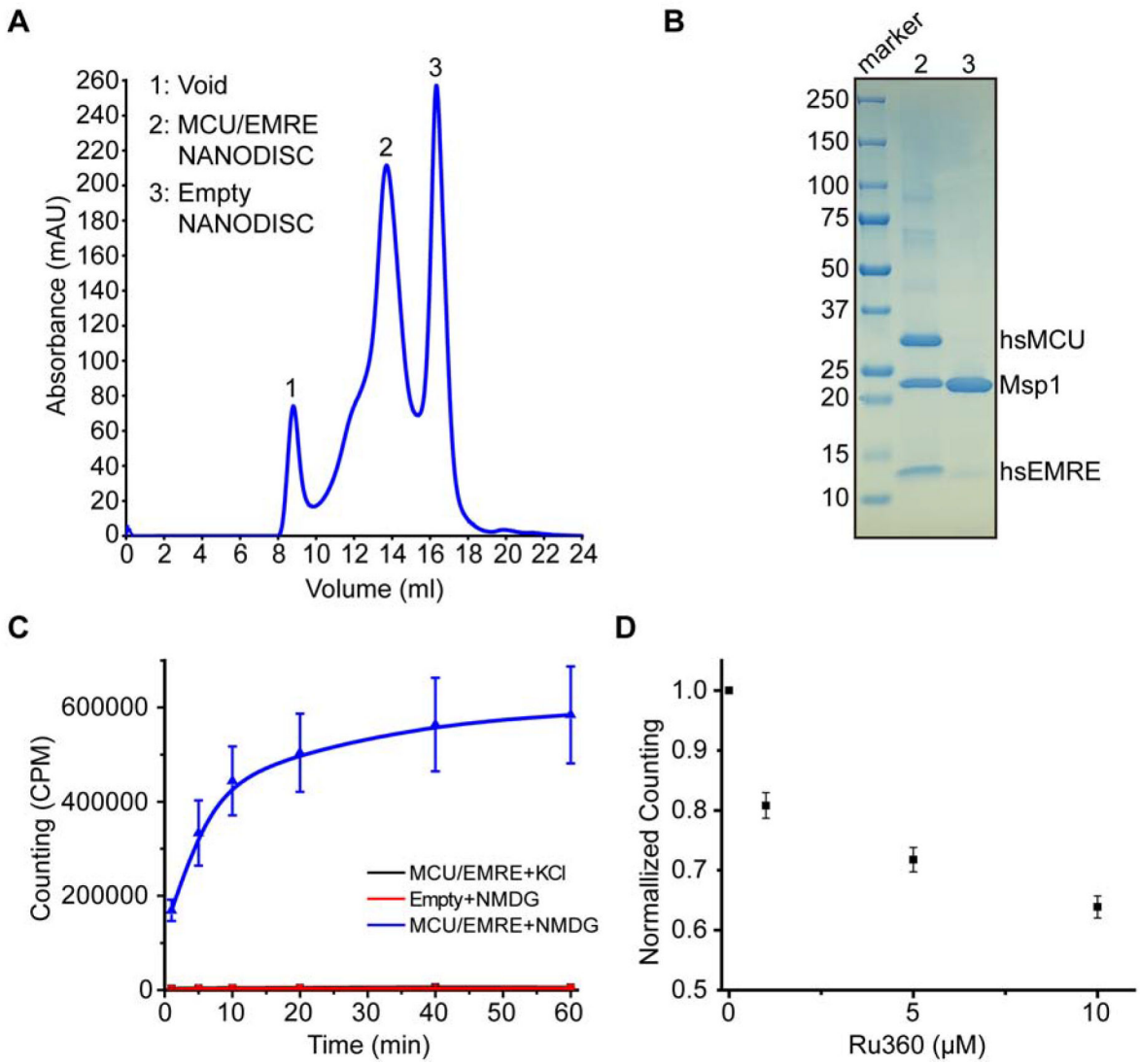

Figure 1. Biochemical and functional characterization of the purified HsMCU/EMRE complex.

(A) Representative size-exclusion chromatography profile of the HsMCU/EMRE complex reconstituted in nanodisc.

(B) Representative SDS-PAGE analysis of the purified HsMCU/EMRE complex in nanodisc with lanes corresponding to peak 2 and 3 of the gel filtration profile shown in **A**.

(C) The purified HsMCU/EMRE complex was reconstituted into liposomes loaded with 150mM KCl and the protein's activity was measured using a radioactive $^{45}Ca^{2+}$ flux assay. Shown here is the time dependent $^{45}Ca^{2+}$ uptake by empty liposomes (red points) or HsMCU/EMRE proteoliposomes incubated with $^{45}Ca^{2+}$ in a reaction buffer containing 150mM NMDG (blue points) or 150mM KCl (black points). The results show that in a reaction solution containing 150mM NMDG and the K^+-selective ionophore valinomycin (to generate an electrical driving force), HsMCU/EMRE proteoliposomes exhibited time-dependent $^{45}Ca^{2+}$ uptake while the same proteoliposomes in a reaction solution containing valinomycin and 150 mM KCl (to eliminate electrical driving force) showed no $^{45}Ca^{2+}$ accumulation, recapitulating the voltage-dependent Ca^{2+} uptake property of the MCU.

(D) Concentration-dependent inhibition of HsMCU/EMRE proteoliposomes by Ru360, demonstrating that Ru360 also blocks HsMCU $^{45}Ca^{2+}$ uptake in a concentration-dependent manner. Each point represents radioactivity measured after 30 min reaction normalized to sample without Ru360. All data in **C** and **D** are shown as mean ± SEM (n = 3 independent experiments). See also Figure S1.

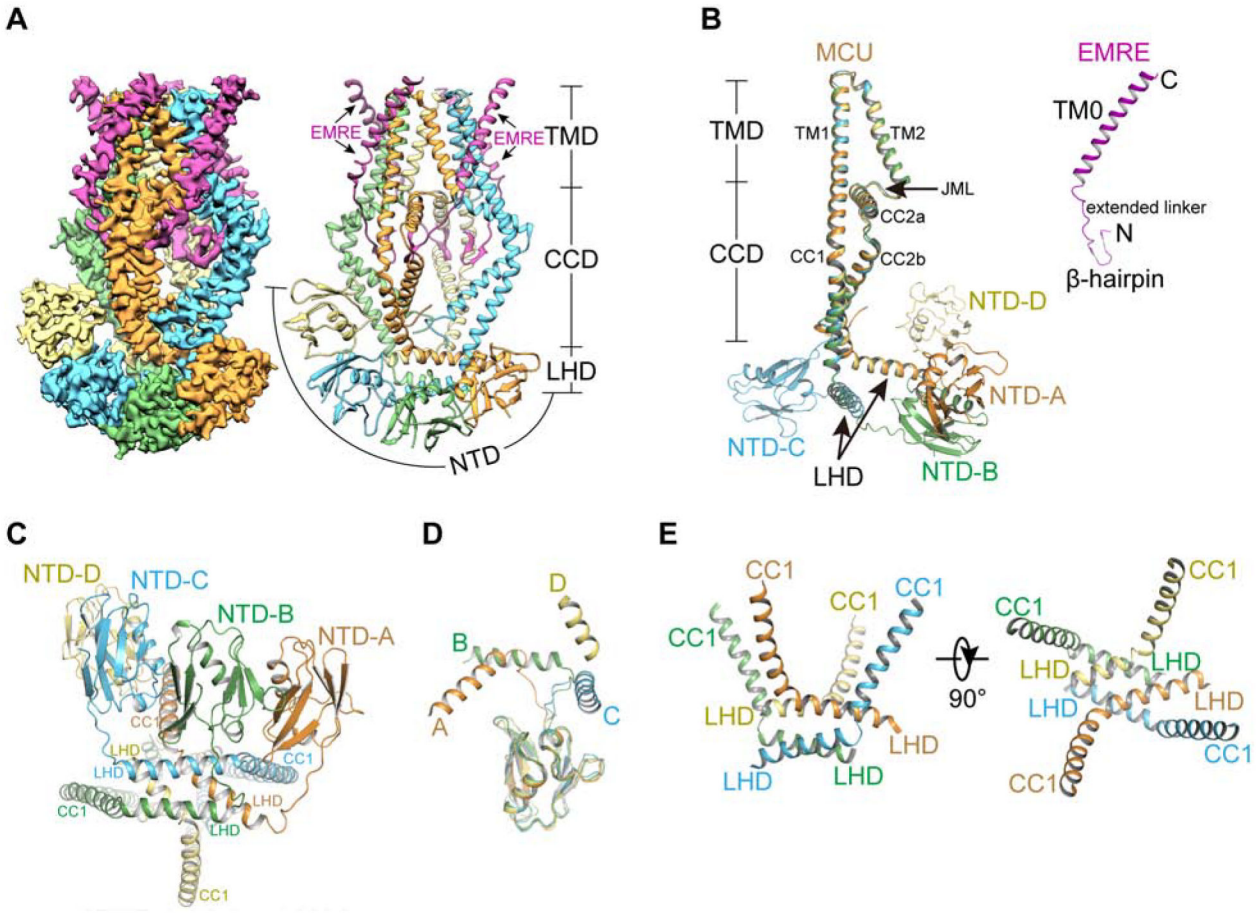

Figure 2. Cryo-EM structure of the HsMCU/EMRE complex.

(A) The cryo-EM map (left) and ribbon diagram (right) of the HsMCU/EMRE complex with each MCU subunit individually colored and EMRE shown in purple.

(B) Structural alignment and domain organization of the four HsMCU subunits (left) with each subunit individually colored. Right, domain organization of HsEMRE.

(C) Bottom view (along the pore axis) of the N-terminal domain (NTD) of HsMCU. The unique side-by-side oligomerization at the NTD is made possible by the linker helix domain (LHD) that is positioned between the NTD and CC1 helix.

(D) Structural alignment of the NTDs of HsMCU. The linker helix from each HsMCU subunit adopts a different orientation to mediate the unique oligomerization at the NTD.

(E) Side (left) and top (right) views of the packing of the linker helices in HsMCU. The CC1 helices are shown for reference.

See also Figures S1, S2, S3, Table S1, and Movie S1.

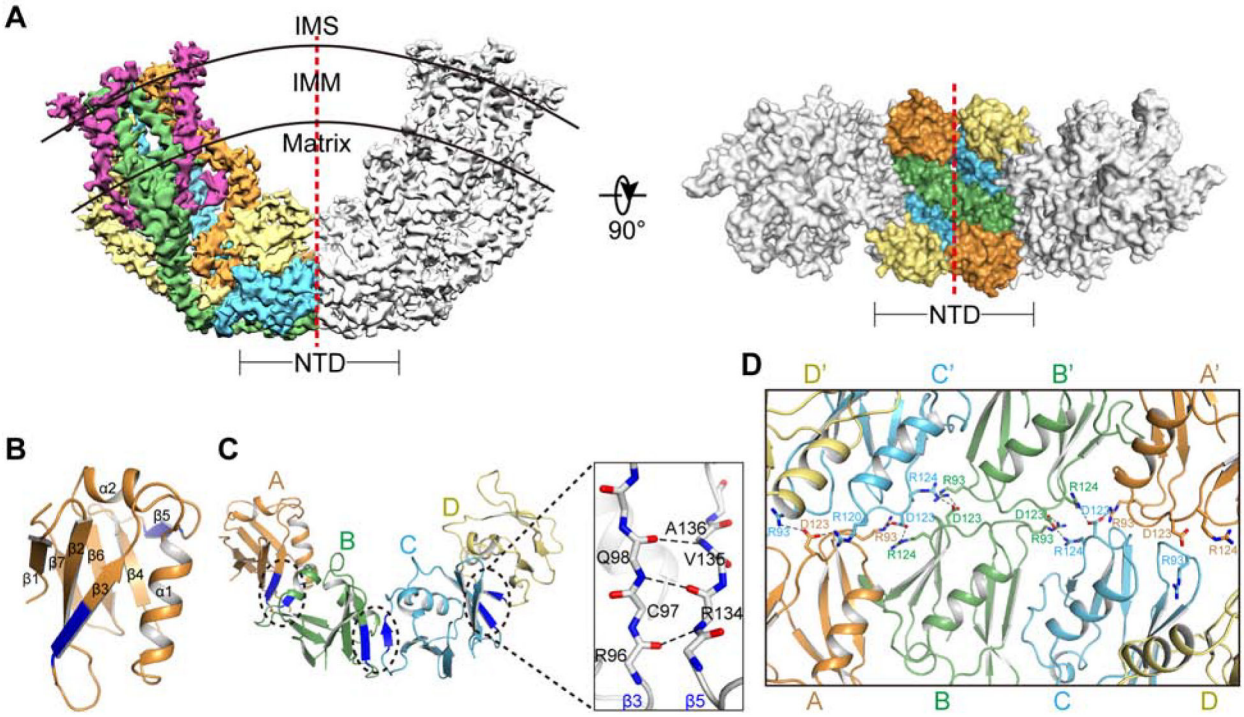

Figure 3. NTD mediated dimerization of HsMCU/EMRE complexes.

(A) Left, side view of the overall cryo-EM map showing two HsMCU/EMRE complexes. Each MCU subunit is individually colored and EMRE is shown in purple in one complex (left) and the other complex is colored in grey (right). Curved lines demarcate the inner mitochondrial membrane boundaries. Dashed line mark the two-fold axis of the two channel tetramers. Right, top view of HsMCU/EMRE complex dimer with the NTDs individually colored. Red dashed line mark the dimerization interface.

(B) Ribbon diagram of a single NTD. Residues on β3 and β5 (blue) participate in inter-subunit interactions.

(C) Tetramerization of the NTDs. Each NTD packs side-by-side, forming an arc, through hydrogen bonding between main-chain atoms on β3 of one subunit and β5 of a neighboring subunit (inset).

(D) The network of electrostatic interactions at the NTD that mediate the dimerization of two HsMCU tetramers.

See also Figures S3, S4, and Movie S2.

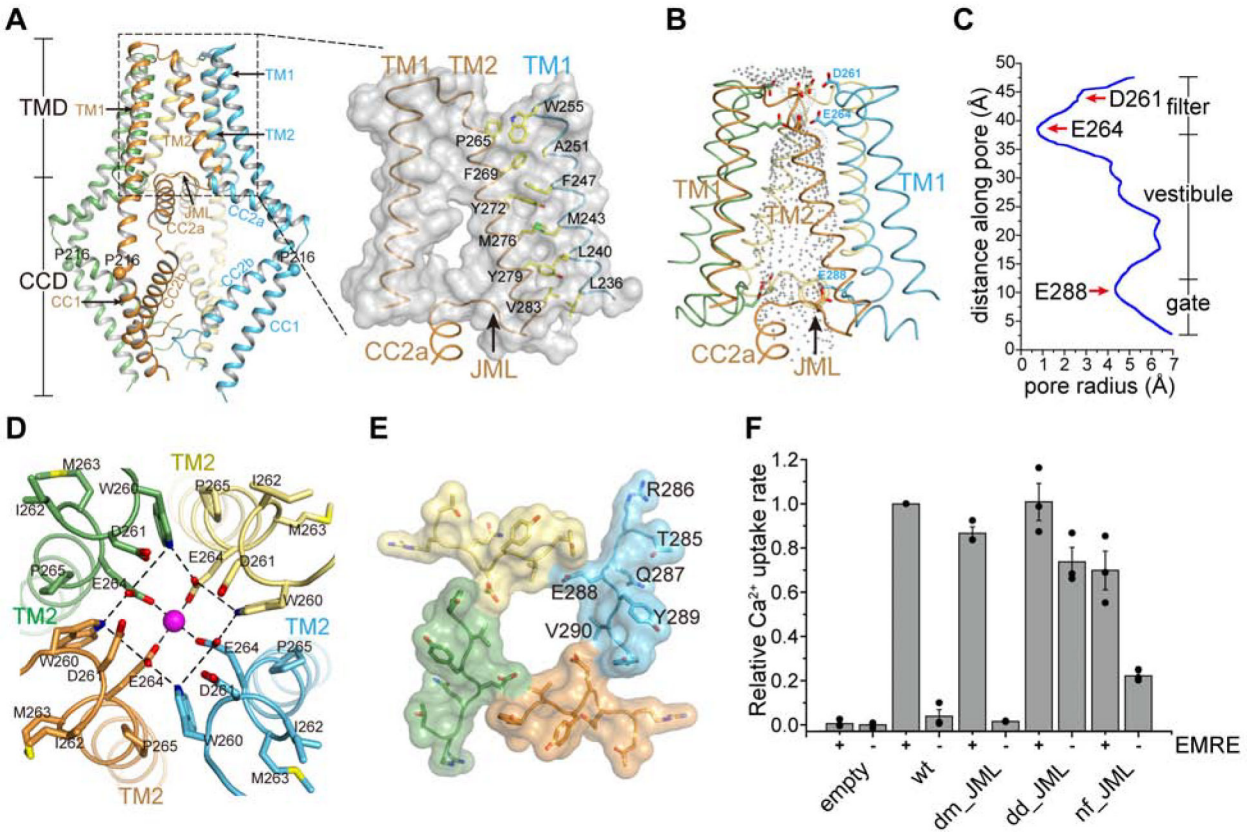

Figure 4. The pore of HsMCU.

(A) The HsMCU pore consists of the TMD and CCD. Colored spheres mark the Cα of P216 that forms an exaggerated bend on CC1 of each subunit. Inset: the surface rendered model of the TMD showing the extensive van der Waals interactions between TM1 of one subunit and TM2 of a neighboring subunit. There is an open gap between TM1 and TM2 within each subunit.

(B) Ribbon diagram of the transmembrane pore with the ion conduction pathway rendered in grey mesh. D261 and E264 of the DIME motif and E288 at the pore exit are shown as sticks; pink sphere represents Ca^{2+}.

(C) Pore radius along the ion conduction pathway.

(D) Top view of the selectivity filter. Dashed lines indicate the hydrogen bond between E264 and W260. The inter-subunit packing between W260 and P265 further stabilizes the selectivity filter of MCU.

(E) Bottom view of the juxtamembrane loop (JML) in HsMCU with E288 and V290 forming the perimeter of the pore exit.

(F) Calcium uptake assay of the JML-swapped HsMCU mutants expressed in $MCU^{-/-}$ (+EMRE) or $MCU^{-/-}/EMRE^{-/-}$ (−EMRE) HEK293 cells. In these mutants, the HsMCU JML was replaced with the MCU JMLs from *D. melanogaster* (dm_JML), *D.discoideum* (dd_JML), or *N.fischeri* (nf_JML). Bar graph shows the rate of calcium uptake normalized to the uptake rate in $MCU^{-/-}$ cells expressing WT HsMCU. Data points shown are mean ± SEM (n=3 independent experiments).

See also Figures S1, S2, and S5.

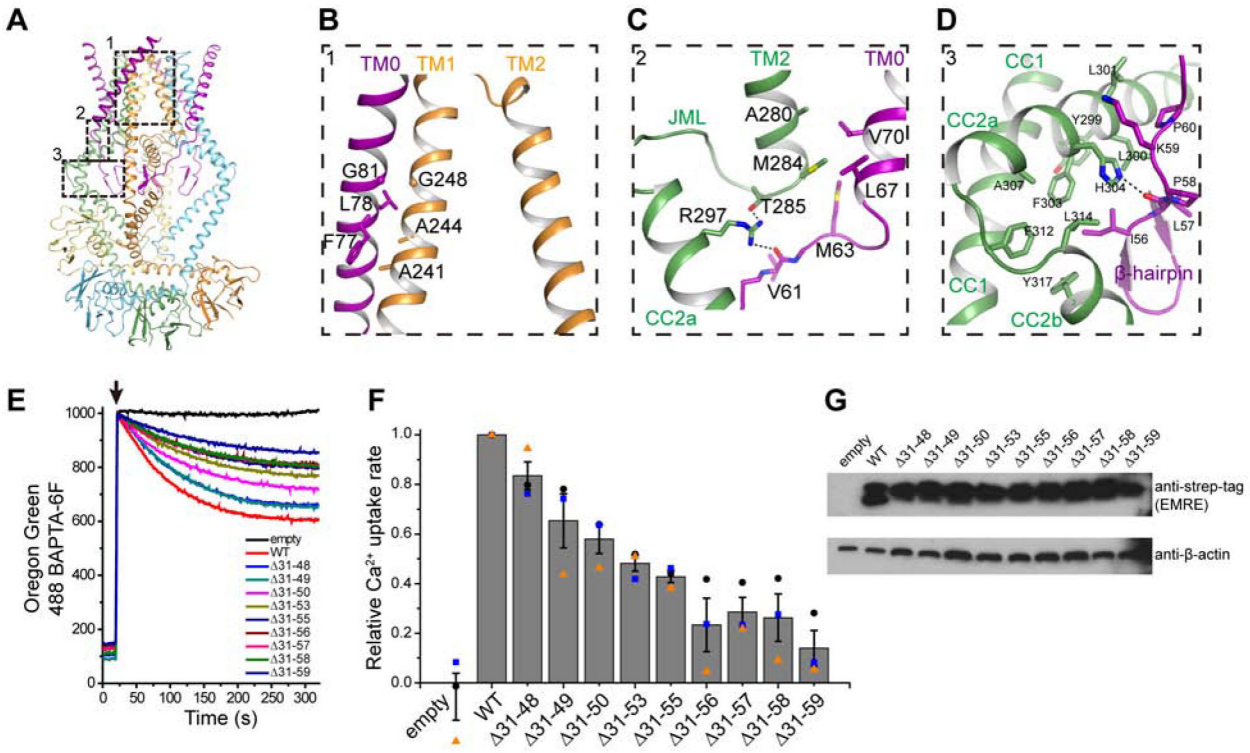

Figure 5. Interactions between MCU and EMRE.

(A) EMRE interacts with MCU at three major loci indicated by numbered boxes.

(B) The atomic interactions between EMRE and MCU at the TMD (box 1).

(C) Interactions between the N-terminal region of EMRE TM0 and MCU's TM2 and JML (box 2).

(D) Interactions between EMRE's β-hairpin and MCU's second coiled-coil (box 3).

(E) Representative fluorescence traces of mitochondrial calcium uptake in EMRE$^{-/-}$ HEK293 cells expressing either wildtype EMRE or mutants with N-terminal truncation. Arrow indicates addition of 60 μM $CaCl_2$ to the reaction.

(F) Bar graph shows the rate of calcium uptake normalized to the uptake rate in cells expressing wildtype EMRE. Data points shown are mean ± SEM (n=3 independent experiments).

(G) Immunoblot of EMRE and its mutants expressed in EMRE$^{-/-}$ HEK293 cells, indicating comparable protein expression in the cells used for the uptake assay. All EMRE constructs carried a C-terminal strep- tag. Mouse anti-β-actin was used as a loading control.

See also Figures 2 and S2.

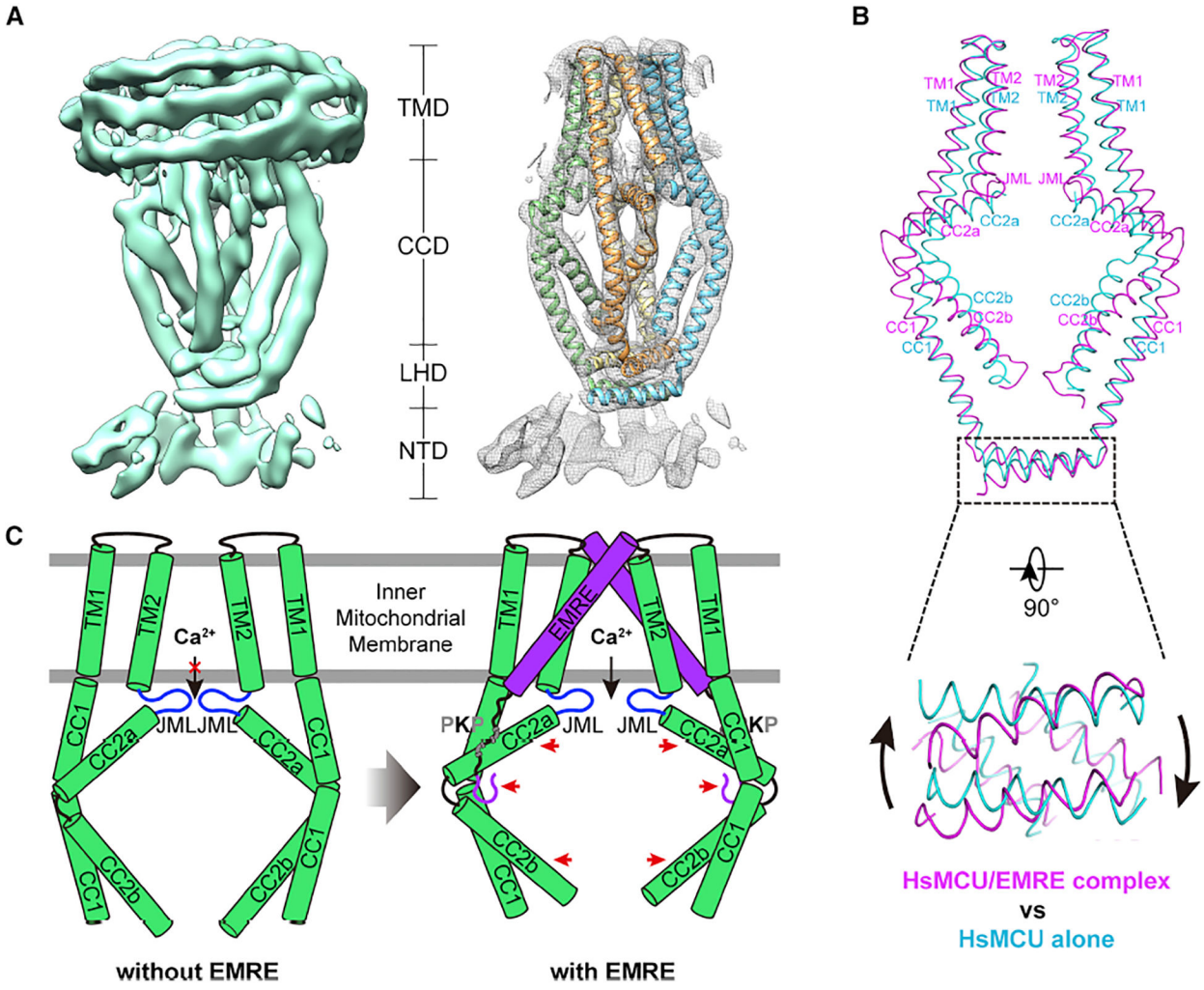

Figure 6. Structural basis of EMRE regulation.

(A) The cryo-EM structure of the HsMCU alone (left, 7.7 Å) with helices from the TMD, CCD and LHD modeled into the electron density (right, nanodisc density is removed for clarity).

(B) Structural alignment of the pore regions of HsMCU between the HsMCU/EMRE complex (pink) and HsMCU alone (cyan) with the front and rear subunits removed for clarity. Inset shows the rotation of the LHD helix-bundle when viewed from the bottom of the channel.

(C) Proposed model of how EMRE regulates the conductivity of MCU. Right, EMRE's β-hairpin and extended linker form a hook that tucks into the fenestration created by CC2a and CC2b and pulls the CC2 helices along with the JML away from the central axis (indicated by red arrows), allowing ions to exit the channel vestibule. In the absence of EMRE (left), CC2 slides toward the central axis and likely dragging the JML with it, thus narrowing the pore exit and causing the inhibition of ion conductivity.

See also Figure S6.